Modelling and Simulation in Materials Science and Engineering 2015, 23(4) (045011)

A combined crystal plasticity and graph-based vertex model of dynamic recrystallization at large deformations

Ylva Mellbin, Håkan Hallberg, Matti Ristinmaa
Division of Solid Mechanics
Lund University, Box 118, S-221 00 Lund, Sweden
ylva.mellbin@solid.lth.se

Abstract

A mesoscale model of microstructure evolution is formulated in the present work by combining a crystal plasticity model with a graph-based vertex algorithm. This provides a versatile formulation capable of capturing finite-strain deformations, development of texture and microstructure evolution through recrystallization. The crystal plasticity model is employed in a finite element setting and allows tracing of stored energy build-up in the polycrystal microstructure and concurrent reorientation of the crystal lattices in the grains. This influences the progression of recrystallization as nucleation occurs at sites with sufficient stored energy and since the grain boundary mobility and energy is allowed to vary with crystallographic misorientation across the boundaries. The proposed graph-based vertex model describes the topological changes to the grain microstructure and keeps track of the grain inter-connectivity. Through homogenization, the macroscopic material response is also obtained. By the proposed modeling approach, grain structure evolution at large deformations as well as texture development are captured. This is in contrast to most other models of recrystallization which are usually limited by assumptions of one or the other of these factors. In simulation examples, the model is in the present study shown to capture the salient features of dynamic recrystallization, including the effects of varying initial grain size and strain rate on the transitions between single-peak and multiple-peak oscillating flow stress behavior. Also the development of recrystallization texture and the influence of different assumptions on orientation of recrystallization nuclei are investigated. Further, recrystallization kinetics are discussed and compared to classical JMAK theory. To promote computational efficiency, the polycrystal plasticity algorithm is parallelized through a GPU implementation that was recently proposed by the authors.

Keywords: Recrystallization, Crystal plasticity, Vertex model, Nucleation, Large deformations, Numerical simulation, Finite elements

DOI: 10.1088/0965-0393/23/4/045011

1 Introduction

The grain microstructure of metallic materials determines macroscopic properties such as strength, ductility and hardness. In order to understand how material properties develop during processing - and in order to device processing conditions to achieve certain properties - reliable simulation models of microstructure evolution are required.

One of the most important processes for controlling the grain size of a material is that of recrystallization (RX), i.e. the formation and growth of new grains with relatively low energy in metals subject to prior or concurrent plastic deformation. The grain growth is driven by minimization of both grain boundary energy and stored energy. For static recrystallization (SRX) this typically takes place when a cold-worked material is kept at an elevated temperature. When the metal is deformed at high temperatures, the increase in stored energy due to plastic deformation will take place in parallel with the stored energy reduction due to nucleation and growth of new grains, a process termed dynamic recrystallization (DRX).

The newly nucleated grains are of low dislocation density, making them softer than the cold worked grains. Thus the recrystallization procedure leads to a decreased flow stress. During DRX repeated recrystallization cycles often lead to a serrated flow stress behavior. The appearance of the oscillations depends on the process parameters since those control the stored energy accumulation due to plastic deformations, as well as stored energy reduction through the formation and growth of new grains. At low strain rates and high temperatures, one recrystallization cycle will have finished before enough stored energy has been built up in the newly recrystallized grains to initiate the next cycle, giving a multi-peak flow stress behavior. With higher strain rates and lower temperatures, enough dislocations will accumulate to allow a new recrystallization cycle to begin before the previous is completed, damping out the oscillations. As the strain rate is increased, several recrystallization cycles will be active at the same time, giving the flow stress curve a plateau-like behavior after the initial peak [1, 2, 3].

As a result of RX processes, the grain structure evolves with significant changes to the grain size distribution. The grain size is an important factor for the macroscopic material behavior, as observed for example by the Hall-Petch relation. Also development of texture is an important aspect of microstructure evolution. As the material deforms, the orientations of the grains change to give the material a texture that depends on the mode of deformation and possibly also on RX processes. While a uniform orientation distribution gives an isotropic material, the changes in crystallographic texture may introduce anisotropy. In simulations of thermomechanical processing it is therefore necessary for the model to be able to capture both the changes in orientation of the grains as well as the nucleation and growth of new grains. In addition, as materials processing in most cases involves large deformations, such as in rolling or extrusion, finite strains need to be considered.

For modeling of recrystallization, there are several different modeling approaches that are commonly used. A more in-depth description of them can be found in the review articles

[4, 5, 6].

Monte Carlo Potts models use probabilistic changes of state variables, defined at the grid points of a fixed grid, in order to minimize system energy. The approach has mainly been used for simulating static recrystallization but has also been applied to dynamic recrystallization in [7]. A drawback with the Monte Carlo Potts method is that there exists no notion of physical time and no real length scale. Cellular automata models are similar to Monte Carlo Potts models in that they are based on state variables defined on a fixed grid, but can be formulated as either stochastic or deterministic and simulations can be performed in physical time and space. The state variables evolve due to physically based switching conditions. There are many examples of cellular automata being used for modeling dynamic recrystallization, both in 2D [8, 9, 10, 11] and in 3D [12]. As both Monte Carlo Potts and cellular automata are formulated on fixed grids, the algorithms are not well suited to describe large deformations or evolution of deformation texture. This is sometimes adressed by linking Monte Carlo Potts and cellular automata models with finite element models [13, 14] and crystal plasticity formulations [15, 16, 17, 18].

The phase field method has also been applied to modeling of dynamic recrystallization, for example in [19]. The grain structure is then described by phase field variables, which typically take one value inside a grain and another outside of the grain, with a continuous variation over the grain boundary. Also phase field formulations have been coupled to finite element models for describing macroscopic mechanical behaviour [20, 21] and to crystal plasticity models [19, 22, 23, 24].

The level set method was introduced in [25] and has been used in mesoscale models of microstructure evolution due to recrystallization [26, 27, 28]. This method is based on the introduction of a level set function for each grain, which is a signed distance function representing the distance to the grain boundary.

Vertex models, also referred to as front tracking models, represent grain boundaries by lines connecting a set of nodes. The state of the microstructure and its evolution is represented by the positions and velocities of these nodes. Vertex models were first used for modeling of grain growth in [29]. The accuracy of the method was improved by the introduction of virtual vertices along the grain boundaries, making it possible to describe grain boundary curvature [30]. In [31], approximations were made to simplify the calculations and in [32] the model was generalized to 3D. Although mostly used for simulating grain growth due to minimization of grain boundary surface energy, nucleation and a driving force based on stored energy was introduced in [33] to permit modeling of recrystallization. A vertex model was also coupled with cellular automata in order to model recrystallization and grain growth in [34]. A benefit with the vertex model, when compared to other models for recrystallization, is the relatively low memory requirements of the implementation.

To achieve a versatile formulation of dynamic recrystallization that is capable of concurrently describing microstructure evolution due to dynamic recrystallization, development of texture and finite-strain deformations, a vertex model is combined with a crystal plasticity

model in the present study. A graph-based vertex algorithm is established to allow convenient tracing of the topology of the grain boundary network and the grain inter-connectivity. This permits physically motivated formulations of aspects such as misorientation-dependent grain boundary energy and mobility and appropriate identification of nucleation sites for recrystallization. The crystal plasticity model contributes the framework for finite strain plasticity, accumulation of stored energy and the evolution of texture. The model is employed in a finite element setting and illustrative simulations are performed to indicate the capabilities of the proposed formulation. Results from the simulation show that the model is capable of capturing many of the prominent features of DRX, such as the effects of strain rate, nucleation rate and initial grain size on the flow stress behavior, as well as of describing the texture evolution of the material.

This paper begins with a thorough description of the proposed model. First the crystal plasticity and the vertex models are presented in sections 2 and 3, respectively. Thereafter, a description of the modeling of recrystallization follows in section 4 and the coupling between the models is described in section 5. Results from computer simulations are presented in section 6 and compared to classical models for recrystallization. Finally, some concluding remarks are given in section 7.

2 Crystal plasticity model

Crystal plasticity models are commonly used to describe the deformation of crystalline solids while also capturing the texture evolution. In crystal plasticity, established in [35, 36, 37], the plastic deformations are described by slip in the crystalline structure. To derive the crystal plasticity model, the general kinetics and thermodynamics of the model is taken as the point of departure. This is followed by a description of the plastic slip deformation and the resolved shear stress. At the end, the specific details of the adopted model are given.

2.1 Kinematic and thermodynamic considerations

To set the framework for the crystal plasticity model, let the motion of a particle in a body at position $\mathbf{X}$ in the reference configuration be described by the function $\varphi(\mathbf{X}, t)$. The deformation gradient $\mathbf{F}$ is then defined as $\mathbf{F} = \partial_X \varphi$.

Given that the model should include nucleation of new, stress free grains in a deformed structure, which will be discussed further in sections 4-5, each grain will be subject to an individual deformation gradient $\mathbf{F}_{\text{gr}}$. Using a multiplicative split of the deformation gradient it follows that

$$\mathbf{F}\mathbf{F}^* = \mathbf{F}_{\text{gr}} \tag{1}$$

where $\mathbf{F}^*$ is related to the deformation at which the grain is stress free. $\mathbf{F}^*$ is constant, i.e. $\dot{\mathbf{F}}^* = 0$. The volume change of a grain between its undeformed configuration and the current configuration is then given by the Jacobian $J = \det(\mathbf{F}_{\text{gr}})$, where $\det(\cdot)$ is the determinant of

a tensor. The deformation gradient for each grain can be split into an elastic part $\mathbf{F}^{\mathrm{e}}$ and a plastic part $\mathbf{F}^{\mathrm{p}}$ as

$$\mathbf{F}_{\mathrm{gr}} = \mathbf{F}^{\mathrm{e}}\mathbf{F}^{\mathrm{p}} \tag{2}$$

cf. [38, 39]. The evolution of the plastic deformation gradient is given by

$$\dot{\mathbf{F}}^{\mathrm{p}} = \mathbf{l}^{\mathrm{p}}\mathbf{F}^{\mathrm{p}} \tag{3}$$

where $\mathbf{l}^{\mathrm{p}}$ is the plastic velocity gradient and a superposed dot denotes the material time derivative. The right Cauchy-Green deformation tensor in the grain is then defined as

$$\mathbf{C} = \mathbf{F}_{\mathrm{gr}}^{\mathrm{T}}\mathbf{F}_{\mathrm{gr}} \tag{4}$$

where $(\cdot)^{\mathrm{T}}$ denotes the transpose of a tensorial quantity, and the elastic right Cauchy-Green deformation tensor is defined as

$$\mathbf{C}^{\mathrm{e}} = \mathbf{F}^{\mathrm{e}\mathrm{T}}\mathbf{F}^{\mathrm{e}} \tag{5}$$

Next, turning to thermodynamic considerations, the Helmholtz free energy, ψ, is assumed to be a function of the elastic right Cauchy-Green deformation tensor and internal variables related to the inelastic process, g^{α}. Denoting the mass density in the reference configuration by ρ_0, and considering isothermal processes, the dissipation inequality takes the form

$$D = \frac{1}{2}\mathbf{S} : \dot{\mathbf{C}} - \rho_0\dot{\psi} \geq 0 \tag{6}$$

where a tensorial contraction over two indices is denoted by $(\cdot) : (\cdot)$. The second Piola-Kirchhoff stress tensor, $\mathbf{S}$, is related to the Cauchy stress tensor, $\boldsymbol{\sigma}$, by

$$\boldsymbol{\sigma} = \frac{1}{J}\mathbf{F}_{\mathrm{gr}}\mathbf{S}\mathbf{F}_{\mathrm{gr}}^{\mathrm{T}} \tag{7}$$

With the above information the dissipation inequality can be rewritten as

$$D = \left(\mathbf{S}^{\mathrm{e}} - 2\rho_0\frac{\partial\psi}{\partial\mathbf{C}^{\mathrm{e}}}\right) : \frac{1}{2}\dot{\mathbf{C}}^{\mathrm{e}} + \boldsymbol{\Sigma}^{\mathrm{e}} : \mathbf{l}^{\mathrm{p}} - \sum_{\alpha=1}^{n} G^{\alpha}\dot{g}^{\alpha} \geq 0 \tag{8}$$

where the second Piola-Kirchhoff stress tensor in the intermediate configuration and the Mandel stress tensor were introduced as

$$\mathbf{S}^{\mathrm{e}} = \mathbf{F}^{\mathrm{p}}\mathbf{S}\mathbf{F}^{\mathrm{p}\mathrm{T}}, \qquad \boldsymbol{\Sigma}^{\mathrm{e}} = \mathbf{C}^{\mathrm{e}}\mathbf{S}^{\mathrm{e}} \tag{9}$$

Furthermore, in (8) the thermodynamic force G^{α} that is conjugated to g^{α}, was identified as

$$G^{\alpha} = \rho_0\frac{\partial\psi}{\partial g^{\alpha}} \tag{10}$$

Requiring that no dissipation should occur during purely elastic processes results in the relations

$$\mathbf{S}^{\mathrm{e}} = 2\rho_0\frac{\partial\psi}{\partial\mathbf{C}^{\mathrm{e}}}, \qquad \boldsymbol{\sigma} = \frac{2}{J}\mathbf{F}^{\mathrm{e}}\rho_0\frac{\partial\psi}{\partial\mathbf{C}^{\mathrm{e}}}\mathbf{F}^{\mathrm{e}\mathrm{T}} \tag{11}$$

providing both the second Piola-Kirchhoff and the Cauchy stress tensor.

2.2 Description of crystal plasticity

In crystal plasticity models, the total deformation is generally viewed to consist of an elastic, recoverable, distortion of the crystal lattice and a plastic, non-recoverable, part due to slip on individual slip systems. The non-recoverable plastic slip is the cause of the stored energy accumulation that provides the driving force for recrystallization. The slip systems generally comprise the close-packed planes and directions in the lattice. For face-centered cubic materials, considered here, this provides 12 slip systems of the type $\{111\}\langle 110\rangle$, see [40].

Each slip system $\alpha = 1, 2...12$ is represented in the reference configuration by the orthonormal vectors $\mathbf{M}^\alpha$ and $\mathbf{N}^\alpha$ which denote the slip direction and the normal to the slip plane of system α, respectively. An isoclinic intermediate configuration will be adopted, cf. [41]. The plastic velocity gradient is calculated through superposition of all crystallographic slip rates according to

$$\mathbf{l}^{\mathrm{p}} = \sum_{\alpha} \dot{\gamma}^\alpha \mathbf{M}^\alpha \otimes \mathbf{N}^\alpha \tag{12}$$

where $\dot{\gamma}^\alpha$ is the slip rate in slip system α, cf. [37]. Since $\mathrm{tr}(\mathbf{l}^{\mathrm{p}}) = 0$ it holds that $\det(\mathbf{F}^{\mathrm{p}}) = 1$, i.e. the volume change is purely elastic, $J = J^{\mathrm{e}} = \det(\mathbf{F}^{\mathrm{e}})$, and the plastic deformation is an isochoric process. Here $\mathrm{tr}(\cdot)$ denotes the trace of a tensor.

Finally, taking advantage of (12) in (8) allows the dissipation inequality to be written as

$$D = \sum_{\alpha=1}^{n} (\tau^\alpha \dot{\gamma}^\alpha - G^\alpha \dot{g}^\alpha) \geq 0 \tag{13}$$

where the resolved shear stress in slip system α was introduced as

$$\tau^\alpha = \mathbf{M}^\alpha \boldsymbol{\Sigma}^{\mathrm{e}} \mathbf{N}^\alpha \tag{14}$$

2.3 Specific model

It is assumed that the Helmholtz free energy can be split into an elastic and a plastic part according to

$$\psi = \psi^{\mathrm{e}} + \psi^{\mathrm{p}} \tag{15}$$

By assuming the elastic part to be dependent on the elastic right Cauchy-Green deformation tensor and the Jacobian, and the plastic part to be dependent on the slip parameters g^α we get

$$\rho_0 \psi(J, \mathbf{C}^{\mathrm{e}}, g^\alpha) = \rho_0 \psi^{\mathrm{e}}(J, \mathbf{C}^{\mathrm{e}}) + \rho_0 \psi^{\mathrm{p}}(g^\alpha) \tag{16}$$

The elastic part is assumed to have the Neo-Hookean form

$$\rho_0 \psi^{\mathrm{e}} = \frac{\kappa}{2} \left(\frac{1}{2}(J^2 - 1) - \ln(J) \right) + \frac{\mu}{2}(J^{-2/3}\mathrm{tr}(\mathbf{C}^{\mathrm{e}}) - 3) \tag{17}$$

where κ and μ are the bulk and shear moduli, respectively. From this, the second Piola-Kirchhoff stress tensor in the intermediate configuration can be identified as

$$\mathbf{S}^{\mathrm{e}} = 2\rho_0 \frac{\partial \psi}{\partial \mathbf{C}^{\mathrm{e}}} = \frac{\kappa}{2}(J^2 - 1)\mathbf{C}^{\mathrm{e}-1} + \mu J^{-2/3}\left(\mathbf{I} - \frac{\mathrm{tr}(\mathbf{C}^{\mathrm{e}})}{3}\mathbf{C}^{\mathrm{e}-1}\right) \tag{18}$$

where $\mathbf{I}$ is the second order identity tensor. Insertion into (14) and taking advantage of $\mathbf{M}^\alpha$ and $\mathbf{N}^\alpha$ being orthogonal, the resolved shear stress can be calculated as

$$\tau^\alpha = \mu \mathbf{M}^\alpha \hat{\mathbf{C}}^{\mathrm{e}} \mathbf{N}^\alpha \tag{19}$$

where $\hat{\mathbf{C}}^{\mathrm{e}} = J^{-2/3}\mathbf{C}^{\mathrm{e}}$ is the isochoric part of the elastic right Cauchy-Green deformation tensor.

Letting the plastic part of the Helmholtz energy assume a quadratic form, cf. [42, 43], it is possible to describe the cross-hardening that occurs between different slip systems. The following expression is considered

$$\rho_0 \psi^{\mathrm{p}} = \frac{1}{2} Q \sum_\alpha \sum_\beta h_{\alpha\beta} g^\alpha g^\beta \tag{20}$$

with $h_{\alpha\beta} = \delta_{\alpha\beta} + q(1 - \delta_{\alpha\beta})$. The ratio between self-hardening and cross-hardening is controlled by the parameter q. Further, it is now possible to identify the thermodynamic quantity G^α as the slip resistance, which is given by

$$G^\alpha = \rho_0 \frac{\partial \psi}{\partial g^\alpha} = Q \sum_\beta h_{\alpha\beta} g^\beta \tag{21}$$

The evolution laws for the slip parameters g^α, controlling the slip rate, are given by

$$\dot{g}^\alpha = (1 - B g^\alpha)\frac{|\tau^\alpha|}{G_r^\alpha}|\dot{\gamma}^\alpha| \tag{22}$$

and the remaining evolution laws for the slip rates $\dot{\gamma}^\alpha$ are given by the power law format

$$\dot{\gamma}^\alpha = \dot{\gamma}_0 \left(\frac{|\tau^\alpha|}{G_r^\alpha}\right)^m \mathrm{sign}(\tau^\alpha) \tag{23}$$

where m is a parameter and where G_r^α is the total slip resistance on the system which is given by the sum

$$G_r^\alpha = G_0 + G^\alpha \tag{24}$$

In (24), G_0 is a constant resulting from lattice friction while G^α is due to dislocation interactions, individual for each slip system.

Finally, by the adopted approach the dissipation inequality in (8) can be rewritten as

$$D = \sum_{\alpha=1}^{n} \left[|\tau^\alpha|\left(1 - \frac{G^\alpha}{G_r^\alpha}\right) + B g^\alpha |\tau^\alpha| \frac{G^\alpha}{G_r^\alpha}\right] |\dot{\gamma}^\alpha| \geq 0 \tag{25}$$

which means that the mechanical dissipation is always positive, as $G_r^\alpha \geq G^\alpha$. Since the rate of plastic work is given by

$$\dot{W}^{\mathrm{p}} = \sum_{\alpha=1}^{n} \tau^\alpha \dot{\gamma}^\alpha \tag{26}$$

the increase in stored energy due to plastic deformation can be calculated as

$$\dot{E} = \dot{W}^{\mathrm{p}} - D = \sum_{\alpha=1}^{n} \tau^\alpha \left(1 - Bg^\alpha\right) \frac{G^\alpha}{G_r^\alpha} \dot{\gamma}^\alpha \tag{27}$$

cf. also [44, 45]. The model given above is the same as used in [46], which in turn is an isothermal variant of that presented in [47].

3 Vertex model

Having covered finite strain deformation and texture evolution in the crystal plasticity formulation, the attention is now turned to the representation and evolution of the grain structure. This is achieved in the present work by representing the microstructure by a vertex model. The vertex method is based on the description of the grain structure through the positions of a set of vertices, which are connected by lines representing grain boundaries. In the first formulations of vertex models, vertices were only located at triple junctions where three grain boundaries meet, but it has since been shown that the introduction of so called virtual vertices, situated along the grain boundaries between triple junctions, increases the accuracy of the model since they introduce effects related to grain boundary curvature. However, in [48] it is argued that the effects of virtual vertices are limited. In the present application we restrict ourself to using only real vertices, in order to keep the required computation times at a minimum, but the model could easily be extended to include virtual vertices as well. To keep track of the grain structure topology, a graph representation is employed.

3.1 Graph representation

A two-dimensional grain structure can be viewed as a number of neighboring polygons. By denoting the grain boundaries as edges and the grain boundary junctions as vertices we obtain a *planar graph* $\boldsymbol{G}$, where each face will correspond to a grain. A planar graph is a graph that can be drawn on a plane (or a sphere) without crossing edges and which can be represented by only straight lines. From $\boldsymbol{G}$ we can construct its dual graph, denoted by $\boldsymbol{G'}$. $\boldsymbol{G'}$ has a vertex on each face in $\boldsymbol{G}$. For each edge e in $\boldsymbol{G}$, there should be a corresponding edge in $\boldsymbol{G'}$, crossing e and connecting the vertices of $\boldsymbol{G'}$ corresponding to the two faces of $\boldsymbol{G}$ on either side of e. Thus the vertices in the dual graph $\boldsymbol{G'}$ will correspond to the grains of the microstructure. Since the dual of a planar graph is again a planar graph, $\boldsymbol{G'}$ can also be drawn on a plane without crossing edges, which is consistent with the notion of edges representing the boundaries between adjacent grains. Keeping track of both $\boldsymbol{G}$ and $\boldsymbol{G'}$ permits formulation

of a model for the grain structure where it is possible to keep track of individual grains. This is usually not done in vertex simulations, but is necessary to allow tracing of which grains are neighbors and for the coupling to crystal plasticity. An example of the representation of a grain structure as a planar graph and its dual is shown in Figure 1.

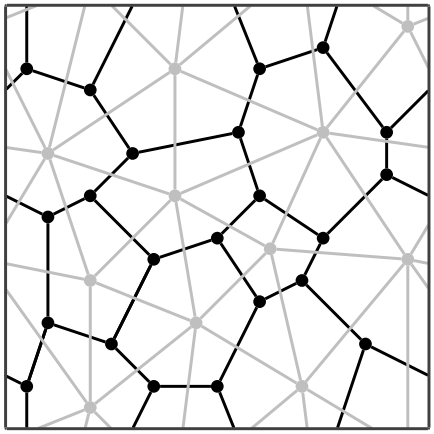

Figure 1: Sketch of the graph representation of a simple grain structure with periodic boundary conditions. The black lines represents the grain boundaries, edges of the graph $\boldsymbol{G}$, and triple junctions, the vertices of $\boldsymbol{G}$. The dual graph $\boldsymbol{G'}$, where the vertices represents the grains, is drawn in gray.

Since no virtual vertices are used in the vertex model, all vertices in $\boldsymbol{G}$ should be connected by three edges. As each vertex in $\boldsymbol{G}$ or $\boldsymbol{G'}$ will have only a few connected edges, storing the structure in an incidence matrix or adjacency matrix would result in a very scarcely populated matrix. Together with the fact that the structure will be continuously updated, this suggests that a linked structure is a good alternative. Such a structure also makes it easy to keep track of the relationship between the graphs.

The fact that a planar graph can be drawn on a sphere as well as on a plane implies that the interpretation of the grain structure as a planar graph and its dual is suitable for use with periodic boundary conditions.

3.2 Topological transformations

As the grain structure evolves it will undergo a number of topological transformations. For example, the recombination of triple points and the removal of shrinking triangular grains are shown in Figure 2. These transformations, often called T1 and T2, are captured by the vertex formulation.

The introduction of a stored energy into the model will introduce topology changes not encountered when the driving force is only due to the minimization of grain boundary energy. This necessitates the introduction of yet another transformation [33]. This transformation, called TA, shown in Figure 3, involves the crossing of a grain boundary segment by a migrating

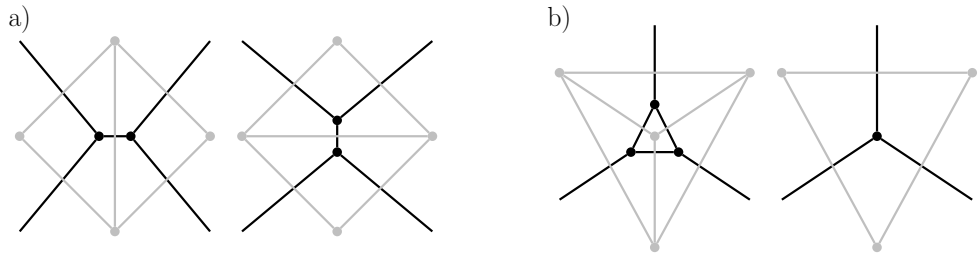

Figure 2: Illustration of typical vertex model transformations; (a) T1 transformation where two triple junctions meet and recombine to form a new grain boundary. (b) T2 transformation where a shrinking grain disappears and three triple junctions merge to form a single vertex. The black lines show the graph $\boldsymbol{G}$ represents the grain boundaries and triple junctions, and the dual graph $\boldsymbol{G'}$, where the vertices represents the grains, is drawn in gray.

vertex.

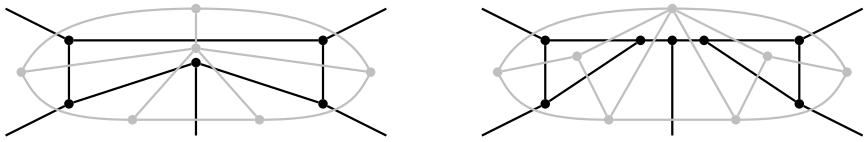

Figure 3: Illustration of a TA transformation where a migrating vertex comes close to a grain boundary, forcing a grain to be split into two grains. The black lines show the graph $\boldsymbol{G}$ represents the grain boundaries and triple junctions, and the dual graph $\boldsymbol{G'}$, where the vertices represents the grains, is drawn in gray.

3.3 Evolution of the vertex model

Evolution of the microstructure is driven by energy minimization. Considering a 2D model and assuming a constant thickness h, the energy of the grain boundaries, $\mathcal{V}_{\mathrm{GB}}$, is calculated as

$$\mathcal{V}_{\mathrm{GB}}(r) = \int_{GBs} \gamma(a) h \mathrm{d}a \tag{28}$$

where a is a coordinate along the grain boundary and $\gamma(a)$ is the grain boundary energy at position a. By integrating the stored energy inside the grains we get the total stored energy $\mathcal{V}_{\mathrm{SE}}$ in the material

$$\mathcal{V}_{\mathrm{SE}} = \int E h \mathrm{d}A \tag{29}$$

where E is the stored energy density per unit volume in the grains. The total energy can be calculated as $\mathcal{V} = \mathcal{V}_{\mathrm{GB}} + \mathcal{V}_{\mathrm{SE}}$. The dissipation function $\mathcal{R}$ due to grain boundary motions can

be expressed as

$$\mathcal{R}(r,v) = \frac{1}{2}\int_{GBs} \frac{v(a)^2}{m_{GB}(a)} h \mathrm{d}a \tag{30}$$

where $v(a)$ is the normal velocity of the grain boundary and $m_{GB}(a)$ is the grain boundary mobility at position a.

By assuming a constant stored energy inside each grain, (29) can be written as

$$\mathcal{V}_{\mathrm{SE}} = h\sum_{G} E_G A_G \tag{31}$$

where E_G is the stored energy density in each grain and A_G the grain area. The grain structure is defined by the positions $\mathbf{r}$ and velocities $\mathbf{v}$ of the vertices. Vertex i has position $\mathbf{r}_i = (x_i, y_i)$ and velocity $\mathbf{v}_i$. The grain boundary between vertex i and j is characterized by the vector $\mathbf{r}_{ij} = (x_{ij}, y_{ij})$ given by $\mathbf{r}_{ij} = \mathbf{r}_i - \mathbf{r}_j$. The normal to $\mathbf{r}_{ij}$ is denoted by $\mathbf{n}_{ij}$ and appears as

$$\mathbf{n}_{ij} = \frac{1}{|\mathbf{r}_{ij}|}\begin{bmatrix} -y_{ij} \\ x_{ij} \end{bmatrix} \tag{32}$$

A point at the grain boundary between vertices i and j with position $\mathbf{r} = \xi\mathbf{r}_i + (1-\xi)\mathbf{r}_j$ has the velocity $\mathbf{v} = \xi\mathbf{v}_i + (1-\xi)\mathbf{v}_j$, which gives the normal velocity $v = \xi\mathbf{v}_i\mathbf{n}_{ij} + (1-\xi)\mathbf{v}_j\mathbf{n}_{ij}$. Using this discretization of the grain structure, the integrals in (28) and (30) can be rewritten as sums over grain boundary sections

$$\mathcal{V}_{\mathrm{GB}} = \frac{1}{2}h\sum_{i=1}^{N}\sum_{j}^{(i)} \gamma_{ij}||\mathbf{r}_{ij}|| \tag{33}$$

$$\mathcal{R} = \frac{1}{6}h\sum_{i=1}^{N}\sum_{j}^{(i)} \frac{||\mathbf{r}_{ij}||}{m_{ij}}[(\mathbf{v}_i\mathbf{n}_{ij})^2 + (\mathbf{v}_j\mathbf{n}_{ij})^2 + (\mathbf{v}_i\mathbf{n}_{ij})(\mathbf{v}_j\mathbf{n}_{ij})] \tag{34}$$

where N is the total number of vertices and γ_{ij} and m_{ij} is the grain boundary energy and mobility, respectively, of the grain boundary between vertices i and j. $\sum_j^{(i)}$ is introduced to denote the sum over all vertices j connected to vertice i.

Since kinetic energy is not considered, the Euler-Lagrange equation, with dissipation forces, then takes the form

$$\frac{\partial\mathcal{R}}{\partial\mathbf{v}_i} + \frac{\partial\mathcal{V}}{\partial\mathbf{r}_i} = 0 \tag{35}$$

from which the equations of motion for the vertices can be found [49]. Together with (31)-(34), (35) provides the following expression for finding the velocities of the vertices

$$\mathbf{D}_i\mathbf{v}_i = \mathbf{f}_i - \frac{1}{2}\sum_{j}^{(i)} \mathbf{D}_{ij}\mathbf{v}_j \tag{36}$$

where $\mathbf{D}_{ij}$ is given by

$$\mathbf{D}_{ij} = \frac{1}{3m_{ij}||\mathbf{r}_{ij}||}\begin{bmatrix} y_{ij}^2 & -x_{ij}y_{ij} \\ -x_{ij}y_{ij} & x_{ij}^2 \end{bmatrix} \tag{37}$$

and $\mathbf{D}_i$ represents the sum

$$\mathbf{D}_i = \sum_j^{(i)} \mathbf{D}_{ij} \tag{38}$$

The driving forces $\mathbf{f}_i$, appearing in (36), are given by

$$\mathbf{f}_i = -\frac{1}{h}\frac{\partial \mathcal{V}}{\partial \mathbf{r}_i} = -\frac{1}{h}\frac{\partial \mathcal{V}_{\mathrm{GB}}}{\partial \mathbf{r}_i} - \frac{1}{h}\frac{\partial \mathcal{V}_{\mathrm{SE}}}{\partial \mathbf{r}_i} \tag{39}$$

where the inclusion of the stored energy is introduced in a similar fashion as in [33]. In addition to the driving force due to grain boundary energy

$$\frac{1}{h}\frac{\partial \mathcal{V}_{\mathrm{GB}}}{\partial \mathbf{r}_i} = \frac{1}{2}\sum_j^{(i)} \gamma_{ij}\frac{\mathbf{r}_{ij}}{||\mathbf{r}_{ij}||} \tag{40}$$

inclusion of the stored energy adds the term

$$\frac{1}{h}\frac{\partial \mathcal{V}_{\mathrm{SE}}}{\partial \mathbf{r}_i} = \frac{1}{2}\sum_j^{(i)} \begin{bmatrix} y_j - y_i \\ x_i - x_j \end{bmatrix} \Delta E_{ij} \tag{41}$$

where ΔE_{ij} is the difference in stored energy between the grains on either side of the grain boundary between vertices i and j. It can be noted, however, that the stored energy is usually not included in vertex models of microstructure evolution despite it being a critical component in, for example, recrystallization processes.

4 Recrystallization model

4.1 Grain boundary properties

Both grain boundary energy and mobility are parameters that are strongly dependent on the local character of the grain boundary in terms of crystallographic misorientation across the interface and the inclination of the boundary plane. For simplicity, however, a scalar misorientation θ is used to characterize grain boundaries in the present model. When calculating θ, symmetry considerations have to be taken into account. For a cubic crystal, there exist 24 equivalent orientations for each given orientation.

By defining the orthogonal rotation matrix $\mathbf{g}$ which aligns a crystal with the reference frame, a matrix representing the misorientation between two crystals i and j can be calculated as $\Delta\mathbf{g}_{ij} = \mathbf{g}_j\mathbf{g}_i^{\mathrm{T}}$. From $\Delta\mathbf{g}_{ij}$, the corresponding scalar misorientation θ is calculated as the minimum misorientation given by the different crystallographically equivalent orientations

$$\theta = \min_{\mathbf{O}_s \in \mathcal{G}_c} \left| \arccos\left(\frac{1}{2}[\mathrm{tr}(\mathbf{O}_s\Delta\mathbf{g}_{ij}) - 1]\right)\right| \tag{42}$$

where $\mathbf{O}_s$ is one of the 24 operators in the cubic symmetry group $\mathcal{G}_c$ [50].

With θ calculated according to (42), the grain boundary energy is assumed to vary according to the Read-Shockley relation

$$\gamma(\theta) = \gamma_{\mathrm{m}} \frac{\theta}{\theta_{\mathrm{m}}} \left(1 - \ln \frac{\theta}{\theta_{\mathrm{m}}}\right) \tag{43}$$

where θ_{m} is the angle differentiating between low and high-angle grain boundaries and γ_{m} is the grain boundary energy for high angle grain boundaries. Here, the standard choice of $\theta_{\mathrm{m}} = 15^\circ$ is made. For $\theta < \theta_{\mathrm{m}}$ the grain boundary energy is taken to vary according to (43) while $\gamma = \gamma_{\mathrm{m}}$ is held constant for $\theta \geq \theta_{\mathrm{m}}$. Turning next to the grain boundary mobility, the formulation in [51] is adopted, providing

$$m(\theta) = m_{\mathrm{m}} \left\{1 - \exp\left[-5 \left(\frac{\theta}{\theta_{\mathrm{m}}}\right)^4\right]\right\} \tag{44}$$

where m_{m} is the mobility of high angle grain boundaries, satisfying $\theta \geq \theta_{\mathrm{m}}$. This expression gives the main characteristics of a low mobility for low angle grain boundaries and a high mobility for high-angle boundaries. It is emphasized that the present model framework puts no restriction on the formulation of grain boundary energy and mobility and arbitrary alternatives to (43) and (44) can be used.

4.2 Nucleation

As a metallic material is plastically deformed, energy will be accumulated in the material through generation and a rearrangement of defects, mainly dislocations. As dislocation networks develop they will tend to form entanglements that subsequently form dislocation cells which, in turn, eventually leads to the formation of subgrains in the grain interiors. These subgrains will be the birthplaces of the recrystallization nuclei [52, 53]. In order for the subgrains to become viable nuclei, however, two criteria need to be met locally in the microstructure. The first is a *kinematic criterion* requiring mobile high-angle grain boundaries to be formed by the nucleation event. The second is a *thermodynamic criterion* requiring a stored energy gradient to be present across the interface that is sufficient to provide enough positive driving pressure for grain growth to occur [54]. These criteria are usually found to be met at grain boundary triple junctions and along grain boundaries [55, 56, 53]. Such sites provide enough lattice curvature and sufficient stored energy differences for providing possible nucleation sites. As nucleation preferentially takes place along pre-existing grain boundaries, it is common to observe so-called *necklace patterns* of recrystallized material along the boundaries. Since the vertex model used in the present work has vertices only at triple junctions, those are the natural places in the topology for nucleation to take place. The vertex representing such a junction will then be split into three vertices, each connecting two of the original grains with the new one, see Figure 4. This change in the microstructure is a reversed T2 transformation, which was shown in Figure 2b.

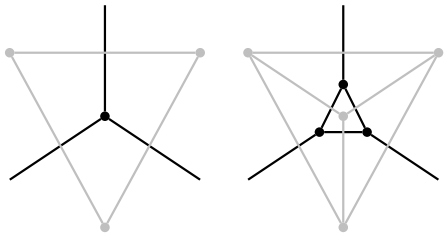

Figure 4: Nucleation of a new grain in the vertex model. The black lines show the graph $\boldsymbol{G}$ represents the grain boundaries and triple junctions, and the dual graph $\boldsymbol{G'}$, where the vertices represents the grains, is drawn in gray.

Being a mesoscale formulation, the present recrystallization model does not resolve the dislocation substructures at finer length-scales. Instead, it is assumed that the necessary subgrain structures have been formed by any preceding plastic deformation and are already present within the grains. The process of subgrain formation is in mesoscale models usually captured by considering an incubation time or a threshold dislocation density, i.e. a threshold stored energy, that needs to be reached before nucleation is initiated [57, 58, 59]. The current formulation is based on defining a threshold value of the stored energy, i.e. of the dislocation density, which is then taken as a local nucleation criterion. Nuclei are added in the computational microstructure at sites where the stored energy is equal to, or greater than, the threshold value. The stored energy is calculated according to (45) in section 5.

During the formation of subgrains, recovery processes very rapidly reduce the dislocation content in the subgrain interiors by annihilation of dislocations and by accumulation of dislocations at the subgrain boundaries. This increases the subgrain misorientation with respect to neighboring regions and eventually provide high-angle, mobile, boundaries. The same processes also provide subgrains with very low internal stored energy. Following the common assumption, recrystallization nuclei are therefore in the present work assumed to be formed with a zero initial dislocation density. This approach, together with the use of a critical dislocation density value for nucleation, ensures that the thermodynamic nucleation criterion is fulfilled.

The crystallographic orientation of the nuclei will influence both the progression of recrystallization and also the evolution of any recrystallization texture in the material [60, 61]. Recrystallization nuclei are products of the cold worked parent material but they do not necessarily inherit their orientation from the parent grains although it is not uncommon that evidence of the texture present in the initial, cold worked, microstructure can be observed also in the recrystallized material [62, 56, 63]. High-angle boundaries with respect to the surrounding material are also required in order to permit growth of the nuclei, causing differences to develop between the initial and recrystallized textures. It can be noted that the development of recrystallization texture is usually attributed to either orientated nucleation or

oriented growth or possibly a combination of these processes [61]. Since the aim of the present study is to establish a tool for simulation of microstructure evolution during recrystallization, two different approaches have been tested. In the first approach the nuclei are given random initial orientations and in the second approach, each new grain is given a 15° misorientation in an arbitrary direction compared to its parent grain. This misorientation corresponds to the situation where a subgrain forms high-angle grain boundaries relative to the parent grain. The parent grain is chosen as the grain at the triple junction having the highest stored energy. However, the present formulation does not pose any restrictions on the initial orientation of the nuclei or on subsequent texture development through oriented nucleation and/or growth. As the grain boundary mobility is taken to depend on the misorientation across the grain boundary in the present model, only nuclei having sufficiently mobile boundaries will grow as new grains. By this approach also the kinetic nucleation criterion is satisfied.

Having defined the initiation of recrystallization, the next question is at what frequency new nucleation events take place. This issue has been approached in a number of ways by different authors. The two main trends is to consider either of *site-saturated nucleation* where all nuclei are assumed to be present at the start of the simulation and no new nuclei are added over time or, alternatively, *continuous nucleation* where new nuclei are continuously added according to some expression of the rate of nucleation. In the latter scenario, both constant and non-constant rates of nucleation have been considered. In the present work, recrystallization nuclei are for simplicity added at a constant rate during the simulation, at sites where the stored energy has reached the threshold value. However, it can be noted that the present model allows arbitrary formulations for the rate of nucleation to be employed.

5 Coupling of the models

The crystal plasticity model described in section 2 is employed in a nonlinear finite element framework although only the material behaviour in a single integration point is considered in the present study. In the integration points within each element, the stresses are calculated by considering the deformations in a large number of grains. The grain structure in each integration point is allowed to evolve, as described by the vertex model, with the deformation and grain orientations supplied from the crystal plasticity model. The crystal plasticity model is used for modelling the deformation and texture evolution of the grain structure and the vertex model is used to represent the evolving topology of the grain structure during recrystallization. Using the common Taylor assumption, introduced in [35], all grains are subjected to the same deformation gradient. The same deformation gradient is also applied to the domain of the vertex model, distorting the initial shape of the area.

A staggered approach is employed where in each time step the crystal plasticity code is first used for calculating stress response and increase in stored energy, after which the vertex model is used to describe the evolution of the grain structure.

Using the expression for the increase in stored energy given in (27), the increment in stored

energy due to crystallographic slip during one time step is calculated in each grain as

$$\Delta E = \sum_{\alpha} \tau^{\alpha} \left(1 - Bg^{\alpha}\right) \frac{G^{\alpha}}{G_r^{\alpha}} \Delta\gamma^{\alpha} \tag{45}$$

The difference in accumulated energy between adjacent grains will then affect the driving force in the vertex model as shown in (41). When the stored energy builds up above the threshold value, new grains will nucleate at triple junctions as discussed in section 4.2. The newly nucleated grains are stress-free and undeformed when they appear. This means that $\mathbf{F}_{\mathrm{gr}} = \mathbf{I}$ when the grain is nucleated, and therefore $\mathbf{F}^{*}$ is given by the inverse of the deformation gradient at the nucleation event, $\mathbf{F}^{*-1} = \mathbf{F}$.

The global stress is calculated as a weighted average over all grains, using their respective areas, A_{gr}, as weight. Thus the stress evolution is dependent both on the crystal plasticity model, giving the stress in each grain, and on the vertex model, controlling the evolution of the grain areas. When calculating the Cauchy stress, it is also important to take into account that the grains are subjected to different deformation tensors providing

$$\boldsymbol{\sigma} = \frac{1}{\sum_{\mathrm{gr}} A_{\mathrm{gr}}} \sum_{\mathrm{gr}} A_{\mathrm{gr}} \frac{1}{J} \mathbf{F}_{\mathrm{gr}} \mathbf{S} \mathbf{F}_{\mathrm{gr}}^{\mathrm{T}} \tag{46}$$

The grain areas are used here as a 2D model of the grain structure is considered, while grain volumes would be used in 3D.

6 Simulation examples

In order to illustrate the capabilities of the proposed model for capturing varying phenomena related to microstructure evolution, several simulations have been performed. To keep the examples small, the microstructure evolution and resulting stress has been studied by deformation of a single integration point. Material parameters for the simulations, summarized in Table 1, have been chosen as representative for pure Cu at around 800K, and have been found from [47, 28].

For simplicity, the grain structure is initialized as a regular structure of hexagonal grains, see Figure 5a. The regular structure is employed to illustrate the capabilities of the model, although it would of course be possible to use alternative initial topologies as well, e.g. created using Voronoi tessellation. For the vertex model, an initial area of $100 \times 100\mu$m is defined with periodic boundary conditions, see Figure 5a. The shape of the area will change as the deformation proceeds.

An initial random texture is given to the polycrystal by generating Bunge-Euler angles (φ_1,Φ,φ_2) according to $\varphi_1 = 2\pi r_1$, $\Phi = \arccos(1 - 2r_2)$ and $\varphi_2 = 2\pi r_3$. Here $r_{1,2,3}$ are random numbers, obtained from a uniform distribution in the interval [0,1]. Apart from in a couple of the simulations studying the texture development, the new nuclei are assigned random orientations generated with this scheme as well. All simulations are performed using a constant nucleation rate, i.e. the total number of nuclei allowed to form per unit time is limited.

Table 1: Material parameters

Parameter	Value	Unit	Description
μ	29	GPa	Shear modulus
κ	62	GPa	Bulk modulus
G_0	27	MPa	Lattice friction
Q	100	MPa	Hardening parameter
m	26		Rate sensitivity
B	8		Parameter controlling saturation of g^α
q	1.4		Ratio between self and cross hardening
$\dot{\gamma}_0$	0.001		Reference slip rate
g_0	0.007		Initial value of g^α
γ_m	0.625	$\mathrm{J/m^2}$	High-angle grain boundary energy
m_m	$6.60 \cdot 10^{-12}$	$\mathrm{m^3/Ns}$	High-angle grain boundary mobility
E_c	$3.61 \cdot 10^5$	$\mathrm{N/m^3}$	Threshold energy for nucleation

6.1 Isochoric deformation

In the first set of simulations, the model has been subjected to an isochoric plane strain deformation described by the deformation gradient

$$\mathbf{F} = \lambda \mathbf{e}_1 \otimes \mathbf{e}_1 + \frac{1}{\sqrt{\lambda}}(\mathbf{e}_2 \otimes \mathbf{e}_2 + \mathbf{e}_3 \otimes \mathbf{e}_3) \tag{47}$$

where a small increment is made to the parameter λ in each time step. The stress-strain plots in this section shows the stress $\sigma = \mathbf{e}_1 \boldsymbol{\sigma} \mathbf{e}_1$ plotted against the logarithmic strain $\ln(\lambda)$. Most simulations have been performed using the relatively low number of 120 crystals at the initial state of the simulations. The grain count is, however, significantly increased through nucleation of new grains during recrystallization as can be seen by comparing Figures 5a and 5c.

Figure 5 shows snapshots of the recrystallization process at different stages. The corresponding places on the flow stress curve and recrystallized fraction are marked in the plots in the right part of the figure. The simulation was run using a strain rate of 0.05 $\mathrm{s^{-1}}$ and the nucleation rate 2500 $\mathrm{s^{-1}}$. As the material is deformed, new grains starts to nucleate along the grain boundaries with random initial orientation. In Figure 5b the necklace-patterns that appear along the grain boundaries as recrystallization is initialized are apparent. The recrystallized grains then continue to grow, as can be seen in Figure 5c, until the original grain structure is completely consumed. Figure 5d shows the fully recrystallized material.

The final grain size distribution is dependent on the process parameters. Figure 6 shows the grain size distributions after recrystallization at different strain rates. These simulations were run with 120 grains present initially, using the nucleation rate 500 $\mathrm{s^{-1}}$, random grain orientation of the nuclei and the strain rates 0.01 $\mathrm{s^{-1}}$, 0.025 $\mathrm{s^{-1}}$ and 0.05 $\mathrm{s^{-1}}$. Higher strain rates lead to smaller grain sizes in the recrystallized material, while lower strain rates mean that the grains have more time to grow before a new nucleation cycle is initiated. In Figure 7 a similar comparison is made for different nucleation rates, all with the strain rate 0.01 $\mathrm{s^{-1}}$

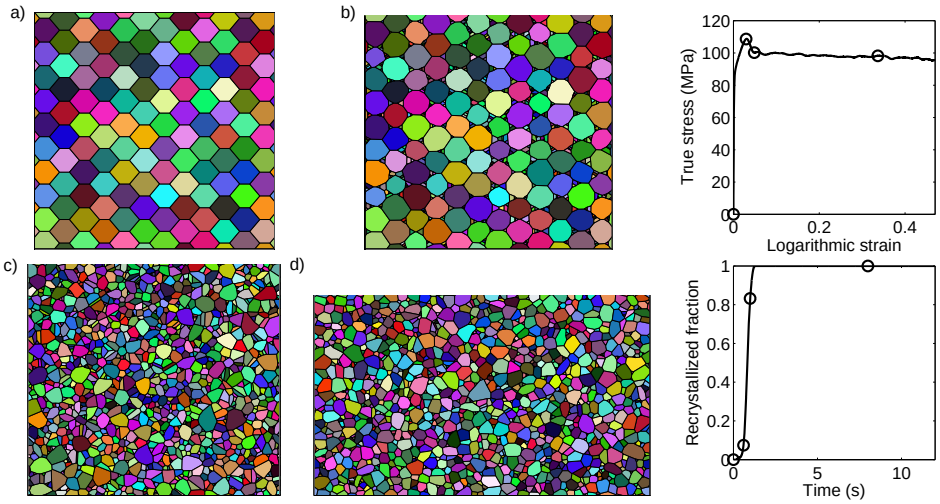

Figure 5: The grain structure (a) before deformation, (b) at the beginning of the recrystallization process, (c) as the recrystallization has progressed and (d) after full recrystallization. The strain and times corresponding to the pictures are marked in the plots to the right.

and 120 grains in the initial grain structure. These simulations show that higher nucleation rates lead to smaller grain sizes in the recrystallized material during the deformation process.

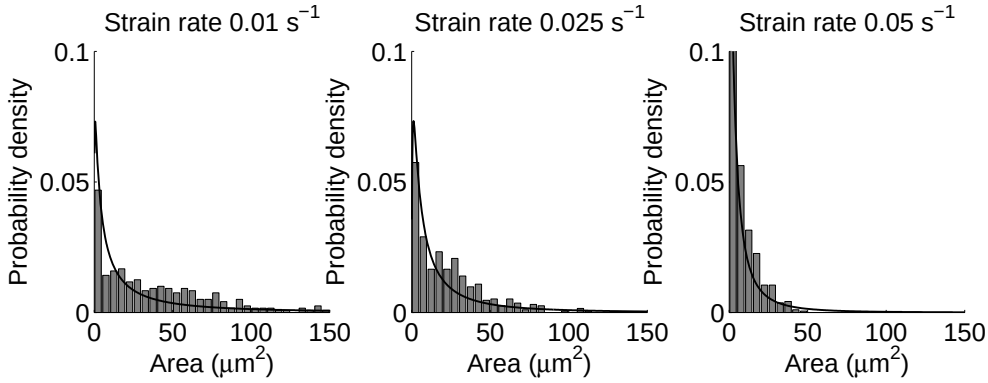

Figure 6: The final grain size distribution for different strain rates. The solid line shows a fitted log-normal distribution.

Figures 8-10 show the flow stress behavior of the material. Random orientation of the new nuclei is used and the initial number of grains is taken to 120. Different strain rates, with the constant nucleation rate 500 s^{-1}, are investigated in Figure 8, showing behavior similar to that reported in [2, 1, 3]. Low strain rates give the oscillating behavior of distinct recrystallization cycles. Higher strain rates make the curve tend toward the single peak behavior typical for a continuous RX process, where a new recrystallization cycle is begun before the previous one is finished. It can also be noted that the peak stress is higher for higher strain rates. A similar

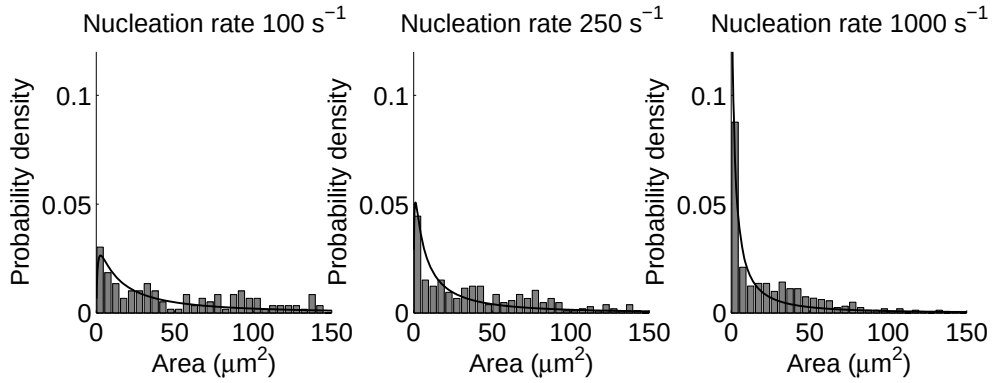

Figure 7: The final grain size distribution for different nucleation rates. The solid line shows a fitted log-normal distribution.

tendency can be seen in Figure 9 which displays the influence of the initial grain size, when the strain rate 0.01 s^{-1} and nucleation rate 500 s^{-1} is used in all simulations. Smaller initial grain sizes yield a lower peak stress and more tendency towards oscillations, in accordance with the experimental observations made in [64, 65].

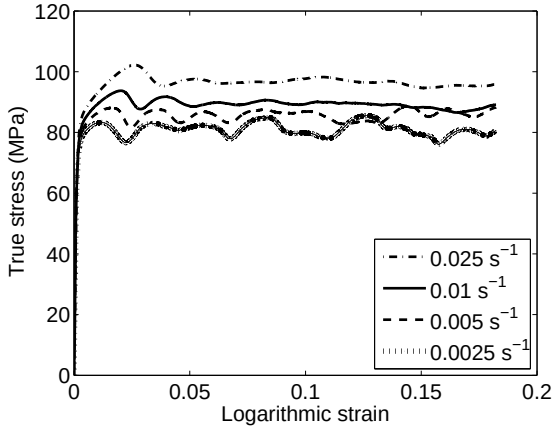

Figure 8: The stress response for different strain rates, with the nucleation rate 500 s^{-1} .

Figure 10 shows the behavior of the flow stress for different nucleation rates, for the strain rate 0.01 s^{-1}, showing less pronounced oscillations for the lower nucleation rate. This is because the lower nucleation rate extends each recrystallization cycle, making the cycles overlap, similar to what is shown in [1]. In Figure 11 the fraction of recrystallized material is plotted over time for different nucleation rates. Here it can also be seen that higher nucleation rates yield steeper recrystallization curves. The dotted lines in Figure 11 have been fitted to the JMAK-function $F = 1 - \exp(-Bt^k)$. This fitting procedure results in Avrami exponents in the range 2.3-2.6, with the lowest exponent for the highest nucleation rate. This can be

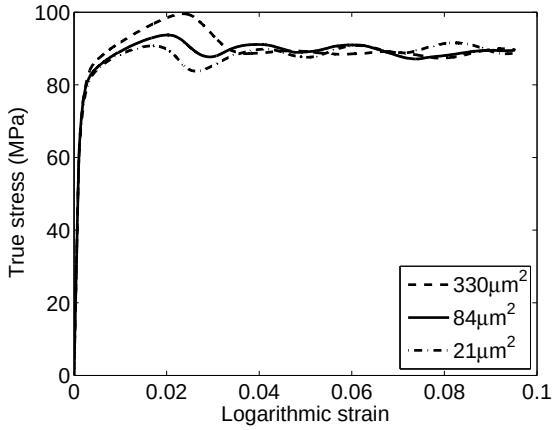

Figure 9: The stress response for different initial grain sizes, with the strain rate 0.01 s^{-1} and nucleation rate 500 s^{-1}.

compared to the theoretical values of 2 for site saturated nucleation and 3 for a constant nucleation rate, which are expected for the 2D conditions currently considered [53].

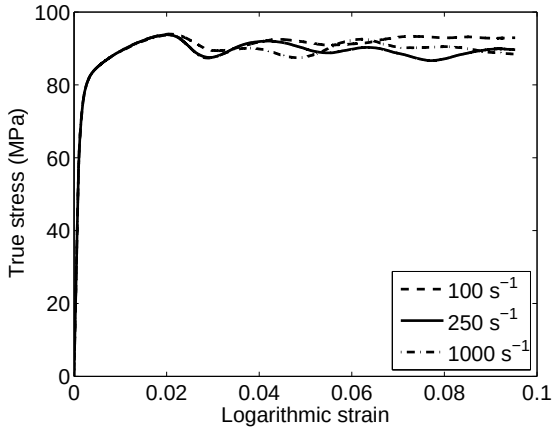

Figure 10: The stress response for different nucleation rates, at the strain rate 0.01 s^{-1}.

A set of simulations to study texture development has been performed with the strain rate 0.05 s^{-1} and nucleation rate 500 s^{-1}, on a structure with 480 initial grains. The initial, fully random, orientation distribution of the material is shown in a {111}-pole figure in Figure 12a. As the material is deformed, the orientations of the grains change depending on the deformation mode. Figure 12b shows the banded texture which develops during deformation given that no recrystallization is taking place. The developing texture is in good agreement with those found in plane strain compression experiments in [66]. The presence of recrystallization will influence the texture development, depending on the orientation of the recrystallized grains. Two different schemes for choosing the orientation of the nuclei have

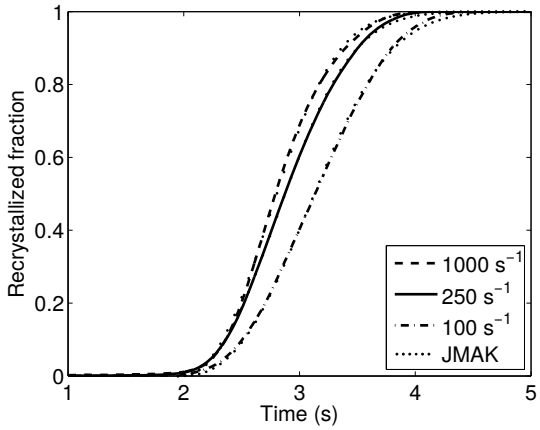

Figure 11: The fraction of recrystallized material plotted against time for different nucleation rates, at the strain rate 0.01 s^{-1}. The steepest curve corresponds to the highest nucleation rate. The dotted lines are fits by the classical JMAK relation.

been investigated. The first one is to simply give the new grain a purely random orientation. This approach preserves the uniform orientation distribution during deformation, as can be clearly seen from Figure 12c. The other approach that has been implemented is to assign each new grain a 15° misorientation in a random direction compared to its parent grain. The result from letting the orientation of the nuclei depend on the parent grain is presented in Figure 12d, indicating that some texture development continues during the recrystallization process, although the resulting texture differs somewhat from that in Figure 12b and is much less pronounced.

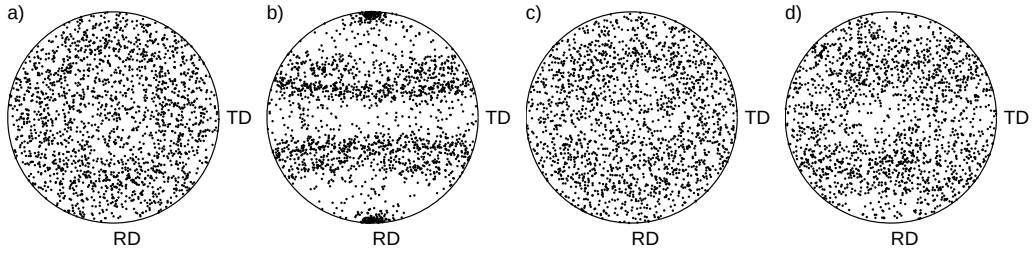

Figure 12: Pole figure showing the {111} poles of the grains (a) before deformation (b) after deformation without recrystallization (c) after deformation with random orientation of nucleated grains and (d) after deformation when the orientation of the nuclei depends on the parent grain orientation. The deformation is imposed according to (47). RD denotes the $\mathbf{e}_1$-direction and TD the $\mathbf{e}_2$-direction.

The different schemes for choosing the orientation of the nuclei were also found to influence the flow stress behavior, as can be seen in Figure 13. In these simulations the nucleation rate

500 s^{-1} is used and the initial number of grains is taken to 120. When compared to the purely random orientation, assigning each new grain a 15° misorientation in a random direction compared to its parent grain gives a higher maximum flow stress. At the beginning of the flow stress curve a double peak can be seen. One possible explanation for this phenomenon might be that the the first peak appears as new grains are at first nucleated around grains where the slip directions are well aligned with the direction of the deformation, which therefore have the largest plastic deformations. When those heavily deformed grains have been consumed, nuclei will start to form with orientations from the grains with less optimal orientations, yielding the second, higher peak. However, over time the orientations giving the largest plastic deformations will become dominant among the newly nucleated grains, resulting in a lowering in the flow stress as the texture develops.

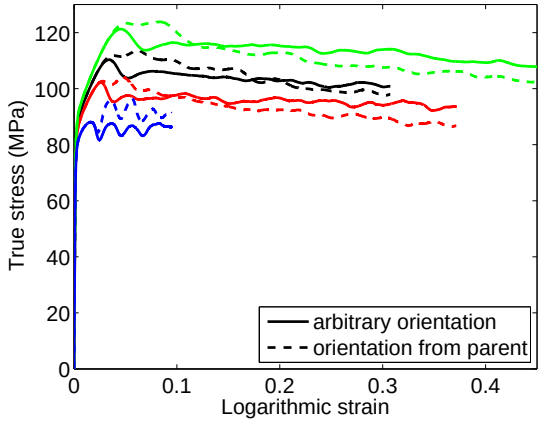

Figure 13: The stress response for different strain rates, with the nucleation rate 500 s^{-1}, for the two different nucleation schemes. The strain rates considered are 0.005 s^{-1}, 0.025 s^{-1}, 0.05 s^{-1} and 0.1 s^{-1}, where the lowest curves corresponds to the lowest strain rate.

6.2 Simple shear

In order to test the model for different deformation modes, the model has also been subjected to simple shear, described by the deformation gradient

$$\mathbf{F} = \gamma \mathbf{e}_1 \otimes \mathbf{e}_2 + \mathbf{I} \tag{48}$$

where a small increment is made to the parameter γ in each time step. The grain structure was initialized with 480 grains, as shown in Figure 14a, with Figure 14b showing the fully recrystallized material. Again, the capability of the proposed model to capture microstructure evolution at finite strain deformations is illustrated.

The texture evolution is also studied in the case of simple shear, as can be seen in Figure 15. The simulations were performed with the strain rate 0.05 s^{-1} and nucleation rate 500

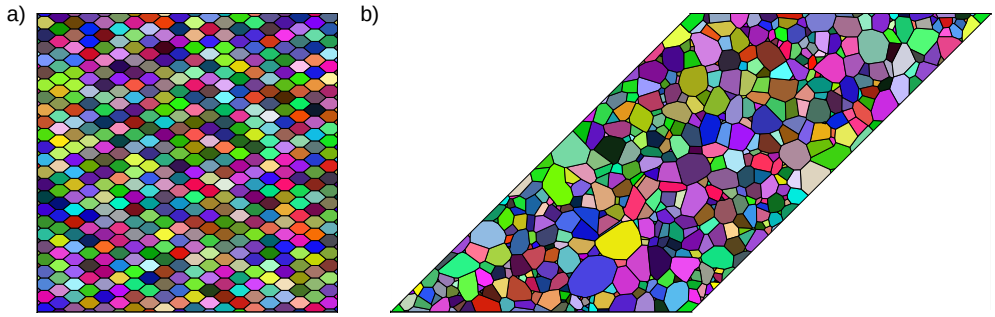

Figure 14: The grain structure (a) before deformation, (b) after full recrystallization.

s^{-1}. When no recrystallization is present the resulting texture, shown in Figure 15b, becomes that typical for simple shear. The texture that is seen to develop in Figure 15b is in very close agreement with the texture found by experimental planar simple shear tests in [66]. Again, giving the new grain a purely random orientation preserves the uniform orientation distribution during deformation, see Figure 15c. Meanwhile, assigning each new grain a 15° misorientation in a random direction compared to its parent grain preserves some traces of the texture development partially during the recrystallization process, as indicated by Figure 15d.

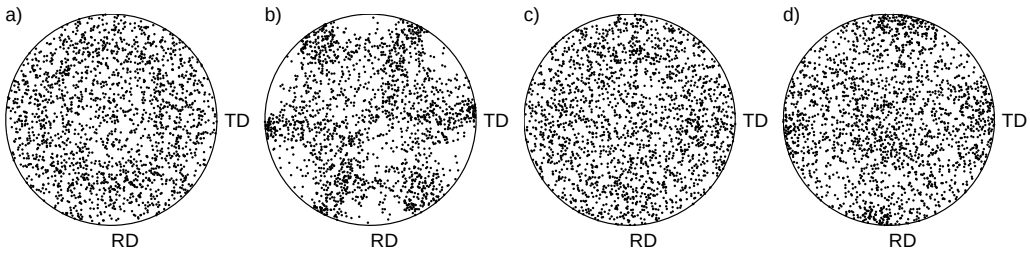

Figure 15: Pole figure showing the {111} poles of the grains for simple shear according to (48). (a) before deformation (b) after deformation without recrystallization (c) after deformation with random orientation of nucleated grains and (d) after deformation when the orientation of the nuclei depends on the parent grain orientation. RD denotes the $\mathbf{e}_1$-direction and TD the $\mathbf{e}_2$-direction.

7 Concluding remarks

The model proposed in the present study has been developed within a finite strain plasticity framework to be able to describe microstructure evolution due to dynamic recrystallization, capturing texture evolution as well as grain size changes. This has been achieved through coupling of a crystal plasticity model and a graph-based vertex model, incorporating the stored energy in the grains as a driving force for the microstructure evolution. Results from the

simulations show that the proposed model is capable of capturing the characteristic features of the dynamic recrystallization process, as well as the texture evolution. The recrystallization kinetics are comparable with results from classical JMAK-theory. The flow stress shows the oscillating behavior typical for DRX, where variations in strain rate, nucleation rate and initial grain sizes affect the transition from a single peak to a serrated flow stress curve. The model is also proven capable of capturing the texture evolution during deformation and recrystallization, showing the influences on the recrystallized texture of the choice of orientations of the nuclei.

Acknowledgment

Y. Mellbin and H. Hallberg gratefully acknowledges funding from the Crafoord foundation under grant number 20130667. M. Ristinmaa acknowledges funding from the Crafoord foundation under grant number 20140800.

References

[1] M.J. Luton and C.M. Sellars. Dynamic recrystallization in Nickel and Nickel-alloys during high temperature deformation. *Acta Metall. Mater.*, 17:1033–1043, 1969.
[2] H. P. Stüwe and B. Ortner. Recrystallization in hot working and creep. *Met. Sci.*, 8(1):161–167, 1974.
[3] T. Sakai, M.G. Akben, and J.J. Jonas. Dynamic recrystallization during the transient deformation of a vanadium microalloyed steel. *Acta Metall. Mater.*, 31(4):631–642, 1983.
[4] A.D. Rollett. Overview of modeling and simulation of recrystallization. *Prog. Mater. Sci.*, 42:79–99, 1997.
[5] M.A. Miodownik. A review of microstructural computer models used to simulate grain growth and recrystallisation in aluminium alloys. *J. Light Met.*, 2:125–135, 2002.
[6] H. Hallberg. Approaches to modeling of recrystallization. *Metals*, 1:16–48, 2011.
[7] P. Peczak and M.J. Luton. A Monte Carlo study of influence of dynamic recovery on dynamic recrystallization. *Acta Metall. Mater.*, 41(1):59–71, 1993.
[8] R.L. Goetz and V. Seetharaman. Modeling of dynamic recrystallization using cellular automata. *Scripta Metall. Mater.*, 38(3):405–413, 1998.
[9] R. Ding and Z.X. Guo. Coupled quantitative simulation of microstructural evolution and plastic flow during dynamic recrystallization. *Acta Mater.*, 49:3163–3175, 2001.
[10] H. Hallberg, M. Wallin, and M. Ristinmaa. Simulation of discontinuous dynamic recrystallization in pure Cu using a probabilistic cellular automaton. *Comp. Mater. Sci.*, 49(1):25–34, 2010.
[11] G. Kugler and R. Turk. Modeling the dynamic recrystallization under multi-stage hot deformation. *Acta Mater.*, 52:4659–4668, 2004.
[12] H. Hallberg, B. Svendsen, T. Kayser, and M. Ristinmaa. Microstructure evolution during dynamic discontinuous recrystallization in particle-containing Cu. *Comp. Mater. Sci.*, 84:327–338, 2014.
[13] Ho Won Lee and Yong-Taek Im. Numerical modeling of dynamic recrystallization during non-isothermal hot compression by cellular automata and finite element analysis. *Int. J. Mech. Sci.*, 52(10):1277–1289, 2010.
[14] H W Lee, S-H Kang, and Y Lee. Prediction of microstructure evolution during hot forging using grain aggregate model for dynamic recrystallization. *Int. J. Precis. Eng. Manuf.*, 15(6):1055–1062, 2014.
[15] D. Raabe and R. C. Becker. Coupling of a crystal plasticity finite-element model with a probabilistic cellular automaton for simulating primary static recrystallization in aluminium. *Model. Simul. Mater. Sci. Eng.*, 8:445–462, 2000.

[16] Y.J. Lan, N.M. Xiao, D.Z. Li, and Y.Y. Li. Mesoscale simulation of deformed austenite decomposition into ferrite by coupling a cellular automaton method with a crystal plasticity finite element model. *Acta Mater.*, 53(4):991–1003, 2005.
[17] D. Svyetlichnyy, J. Majta, K. Muszka, and Ł. Łach. Modeling of microstructure evolution of bcc metals subjected to severe plastic deformation. *AIP Conference Proceedings*, 1315(1):1473–1475, 2011.
[18] W. Chuan, Y. He, and L. H. Wei. Modeling of discontinuous dynamic recrystallization of a near-α titanium alloy imi834 during isothermal hot compression by combining a cellular automaton model with a crystal plasticity finite element method. *Comp. Mater. Sci.*, 79:944–959, 2013.
[19] T. Takaki, Y. Hisakuni, T. Hirouchi, A. Yamanaka, and Y. Tomita. Multi-phase-field simulations for dynamic recrystallization. *Comp. Mater. Sci.*, 45:881–888, 2009.
[20] T. Takaki, C. Yoshimoto, A. Yamanaka, and Y. Tomita. Multiscale modeling of hot-working with dynamic recrystallization by coupling microstructure evolution and macroscopic mechanical behavior. *Int. J. Plasticity*, 52:105–116, 2014.
[21] C. Yoshimoto and T. Takaki. Multiscale hot-working simulations using multi-phase-field and finite element dynamic recrystallization model. *ISIJ Int.*, 54(2):452–459, 2014.
[22] T. Takaki and Y. Tomita. Static recrystallization simulations starting from predicted deformation microstructure by coupling multi-phase-field method and finite element method based on crystal plasticity. *Int. J. Mech. Sci.*, 52:320–328, 2010.
[23] G. Abrivard, E. P. Busso, S. Forest, and B. Appolaire. Phase field modelling of grain boundary motion driven by curvature and stored energy gradients. part ii: application to recrystallisation. *Phil. Mag.*, 92(28-30):3643–3664, 2012.
[24] L Chen, J Chen, RA Lebensohn, YZ Ji, TW Heo, S Bhattacharyya, K Chang, S Mathaudhu, ZK Liu, and L-Q Chen. An integrated fast fourier transform-based phase-field and crystal plasticity approach to model recrystallization of three dimensional polycrystals. *Comput. Method. Appl. M.*, 285:829–848, 2015.
[25] S. Osher and J.A. Sethian. Fronts propagating with curvature dependent speed: Algorithms based on Hamilton-Jacobi formulations. *J. Comput. Phys.*, 79:12–49, 1988.
[26] M. Bernacki, H. Resk, T. Coupez, and R.E. Logé. Finite element model of primary recrystallization in polycrystalline aggregates using a level set framework. *Model. Simul. Mater. Sci. Eng.*, 17:1–22, 2009.
[27] M. Bernacki, R.E. Logé, and T. Coupez. Level set framework for the finite-element modelling of recrystallization and grain growth in polycrystalline materials. *Scripta. Mater.*, 64:525–528, 2011.
[28] H. Hallberg. A modified level set approach to 2D modeling of dynamic recrystallization. *Model. Simul. Mater. Sci. Eng.*, 21(8):085012, 2013.
[29] A. Soares, A.C. Ferro, and M.A. Fortes. Computer simulation of grain growth in a bidimensional polycrystal. *Scripta Metall. Mater.*, 19:1491–1496, 1985.
[30] H.J. Frost, C.V. Thompson, C.L. Howe, and J. Whang. A two-dimensional computer simulation of capillarity-driven grain growth: Preliminary results. *Scripta Metall. Mater.*, 22:65–70, 1988.
[31] K. Kawasaki, T. Nagai, and K. Nakashima. Vertex models for two-dimensional grain growth. *Phil. Mag. B*, 60(3):399–421, 1989.
[32] K. Fuchizaki, T. Kusaba, and K. Kawasaki. Computer modelling of three-dimensional cellular pattern growth. *Phil. Mag. B*, 71(3):333–357, 1995.
[33] K. Piękoś, J. Tarasiuk, K. Wierzbanowski, and B. Bacroix. Generalized vertex model of recrystallization – Application to polycrystalline copper. *Comp. Mater. Sci.*, 42:584–594, 2008.
[34] M. Zeng and G. Gottstein. The combination of cellular automata model with vertex model for simulation of normal grain growth. *Aluminium*, 78(10):878–880, 2002.
[35] G. I. Taylor. Plastic Strain in Metals. *J. Inst. Metals*, 62:307–324, 1938.
[36] R.J. Asaro and A. Needleman. Texture development and strain hardening in rate dependent polycrystals. *Acta Metall. Mater.*, 33(6):923–953, 1985.
[37] J. R. Rice. Inelastic constitutive relations for solids: an internal-varible theory and its applications to metal plasticity. *J. Mech. Phys. Solids*, 19:433–455, 1971.
[38] E. Kröner. Allgemeine Kontinuumstheorie der Versetzungen und Eigenspannungen. *Arch. Ration.*

Mech. An., 4(1):273–334, January 1959.
[39] E.H. Lee. Elastic-plastic deformation at finite strains. *J. Appl. Mech.*, 36:1–6, 1969.
[40] L. Anand. Single-crystal elasto-viscoplasticity: applications to texture evolution in polycrystalline metals at large strain. *Comput. Method. Appl. M.*, 193:5359–5383, 2004.
[41] J. Mandel. Plasticite classique et viscoplasticity. In *CISM Course No. 97*. Springer-Verlag, Udine., 1971.
[42] L. Méric, P. Poubanne, and G. Cailletaud. Single crystal modeling for structural calculations: Part 1 - Model presentation. *J. Eng. Mater.-T. ASME*, 113(1):162–1701, 1991.
[43] E. P. Busso and G. Cailletaud. On the selection of active slip systems in crystal plasticity. *Int. J. Plasticity*, 21(11):2212 – 2231, 2005.
[44] N. S. Ottosen and M. Ristinmaa. *The Mechanics of Constitutive Modeling*. Elsevier, first edition, 2005.
[45] M. Ristinmaa, M. Wallin, and N. S. Ottosen. Thermodynamic format and heat generation of isotropic hardening plasticity. *Acta Mech.*, 194(1):103–121, 2007.
[46] Y. Mellbin, H. Hallberg, and M. Ristinmaa. Accelerating crystal plasticity simulations using GPU multiprocessors. *Int. J. Numer. Meth. Eng.*, 100(2):111–135, 2014.
[47] P. Håkansson, M. Wallin, and M. Ristinmaa. Prediction of stored energy in polycrystalline materials during cyclic loading. *Int. J. Solids Struct.*, 45(6):1570–1586, 2008.
[48] C. Maurice. Numerical modelling of grain growth: current status. In *Recrystallization and Grain Growth*, pages 123–134. Proceedings of the First Joint International Conference, Springer-Verlag, Berlin, June 2001.
[49] D. Weygand, Y. Bréchet, and J. Lépinoux. A vertex dynamics simulation of grain growth in two dimensions. *Phil. Mag. B*, 78:329–352, 1998.
[50] H. Hallberg. Influence of anisotropic grain boundary properties on the evolution of grain boundary character distribution during grain growth – a 2D level set study. *Model. Simul. Mater. Sci. Eng.*, 22(8):085005, 2014.
[51] F.J. Humphreys. A unified theory of recovery, recrystallization and grain growth, based on stability and growth of cellular microstructures - II. The effect of second-phase particles. *Acta Mater.*, 45(12):5031–5039, 1997.
[52] R.D. Doherty, D.A. Hughes, F.J. Huphreys, J.J. Jonas, D. Juul Jensen, M.E. Kassner, W.E. King, T.R. McNelley, H.J. McQueen, and A.D. Rollett. Current issues in recrystallization: a review. *Mater. Sci. Eng.*, A238:219–274, 1997.
[53] F.J. Humphreys and M. Hatherly. *Recrystallization and related annealing phenomena*. Pergamon, New York, second edition, 2004.
[54] G. Gottstein and L.S. Schvindlerman. *Grain Boundary Migration in Metals*. CRC Press, 2010.
[55] M.C. Theyssier and J.H. Driver. Recrystallization nucleation emchanism along boundaries in hot deformed Al bicrystals. *Mater. Sci. Eng. A*, 272:73–82, 1999.
[56] T.J. Sabin, G. Winther, and D. Juul Jensen. Orientation relationship betweenr ecrystallization nuclei at triple junctions and deformed structures. *Acta Mater.*, 51:3999–4011, 2003.
[57] R. Sandström and R. Lagneborg. A model for hot working occurring by recrystallization. *Acta Metall. Mater.*, 23:387–398, March 1975.
[58] W. Roberts and B. Ahlbom. A nucleation criterion for dynamic recrystallization during hot working. *Acta Metall. Mater.*, 26:801–813, 1978.
[59] P. Bernard, S. Bag, K. Huang, and R.R. Logé. A two-site mean field model of discontinuous dynamic recrystallization. *Mater. Sci. Eng. A*, 528:7357–7367, 2011.
[60] W.B. Hutchinson. Development of textures in recrystallization. *Met. Sci.*, 8:185–196, 1974.
[61] R.D. Doherty. Recrystallization and texture. *Prog. Mater. Sci.*, 42:39–58, 1997.
[62] H.W.F. Heller, C.A. Verbraak, and B.H. Kolster. Recrystallization at grain boundaries in deformed copper bicrystals. *Acta Metall. Mater.*, 32(9):1395–1406, 1984.
[63] A.W. Larsen, H.F. Poulsen, L. Margulies, C. Gundlach, Q. Xing, X. Huang, and D. Juul Jensen. Nucleation of recrystallization observed in situ in the bulk of a deformed material. *Scripta. Mater.*, 53:553–557, 2005.
[64] M. El Wahabi, L. Gavard, F. Montheillet, J.M. Cabrera, and J.M. Prado. Effect of initial grain size

on dynamic recrystallization in high purity austenitic stainless steels. *Acta Mater.*, 53(17):4605–4612, 2005.

[65] T. Sakai. Dynamic recrystallization microstructures under hot working conditions. *J. Mater. Process. Technol.*, 53:349–361, 1995.

[66] C. A. Bronkhorst, S. R. Kalidindi, and L. Anand. Polycrystalline plasticity and the evolution of crystallographic texture in fcc metals. *Phil. Trans. R. Soc. Lond. A*, 341(1662):443–477, 1992.